Journal of Solid State Chemistry **159,** 149–162 (2001)
doi:10.1006/jssc.2001.9144, available online at http://www.idealibrary.com on IDEAL®

Hydrogen Impurity Effects. A_5Tt_3 Intermetallic Compounds between A = Ca, Sr, Ba, Eu and Tt = Si, Ge, Sn with Cr_5B_3-like Structures that are Stable Both as Binary and as Ternary Hydride and Fluoride Phases

E. Alejandro Leon-Escamilla and John D. Corbett[1]

Department of Chemistry and Ames Laboratory—DOE,[2] Iowa State University, Ames, Iowa 50011

Received November 16, 2000; in revised form March 7, 2001; accepted March 15, 2001; published online May 11, 2001

All of the binary systems Ca, Sr, Ba, or Eu (A) with Tt (tetrel) = Si or Ge as well as Sr–Sn form both binary Cr_5B_3-type A_5Tt_3 phases and the corresponding ternary hydrides with stuffed Cr_5B_3- (Ca_5Sn_3F-) type structures. All of those tested, Ca–Si, Ba–Si, Ca–Ge, also yield the isotypic $A_5Tt_3F_x$ phases. The tetragonal structures of Ca_5Si_3, $Ca_5Si_3F_{0.42}$, Sr_5Si_3, $Eu_5Si_3H_x$, Ca_5Ge_3, $Ca_5Ge_3H_x$, $Ca_5Ge_3F_{0.66}$ ($I4/mcm$, No. 140) and of $Ba_5Si_3F_{0.16}$ ($P4/ncc$, Ba_5Si_3-type) were refined from single-crystal X-ray diffraction data. The interstitial H, F atoms are bound in a constricted tetrahedral $(A^{2+})_4$ cavity in the Cr_5B_3-type heavy atom structure, which can be described ideally as $(A^{2+})_5(Tt_2)^{6-}(Tt)^{4-}$. Many of 14 previous reports of the phases reported here were apparently hydrides according to lattice constant differences or, for Sr_5Si_3, the fractional coordinates of Sr2 about the tetrahedral site. An articulated model is developed that allows description of the relationship between the dimensions of the tetrahedral interstitial site and the cation cavity about Tt_2 and for some matrix effects in this structure type. The model suggests limitations on the stability of these binary A_5Tt_3 compounds for the heavier tetrels, as observed. The resistivities of Ca_5Ge_3 and $Ca_5Ge_3H_x$ are both characteristic of poor metals, and Pauli-like magnetic susceptibilities are exhibited by Ca_5Ge_3, $Ca_5Ge_3H_x$, $Ca_5Ge_3F_{0.66}$, Sr_5Ge_3, and Sr_5Sn_3. The characteristic ideal Tt_2^{6-} dimers are evidently not realistic descriptions for these phases; rather at least some of the π^{*4} electrons in the dimers are delocalized in a conduction band. This effect appears to be greater in two europium salts. Bond lengths of dimers in the Ca–Si and Ca–Ge families appear to shorten slightly in three instances of their oxidation to form the hydride or the fluoride, as might be expected.

[1]To whom correspondence should be addressed. E-mail: jcorbett@iastate.edu.

[2]This research was supported by the Office of the Basic Energy Sciences, Materials Sciences Division, U. S. Department of Energy. The Ames Laboratory is operated by DOE by Iowa State University under Contract No. W-7405-Eng-82. Accordingly, the U.S. Government retains a nonexclusive, royalty-free license to publish or reproduce the published form of the contribution, or to allow others to do so for U.S. Government purposes.

Key Words: **hydrogen impurities; Cr_5B_3-type structures; alkaline-earth metal triels A_5Tr_3; structures of Cr_5B_3-type phases; synthesis of Cr_5B_3-type compounds; interstitial binding of H^-, F^-.**

1. INTRODUCTION

Compounds formed between alkali, alkaline-earth, or rare-earth metals and the main group p-elements have been major features in the development of diverse structural and bonding aspects of solid state chemistry. The main-group components most often feature the tetrels (Si family, Tt), pnictogens (P family principally), and chalcogens. One common feature of many of these products is the predominance of valence or closed shell compounds, the so-called Zintl phases (1), although many of these have been so classified solely on the basis of their structures (2). Contradictions or inconsistencies between our results and those in literature, or, equally often, an inability to obtain a reported compound in high yield, have repeatedly forced us into a consideration of phase stabilization via unrecognized impurities. Carbon, nitrogen, and oxygen are naturally common candidates, but hydrogen has turned out to be a particularly pervasive problem, both because its presence is usually not seriously considered and the fact that the atom is essentially undetected in heavy atom compounds by common X-ray diffraction methods for phase detection or analysis.

Our first systematic exploration stemmed from an inability to sort out the formation of Mn_5Si_3- from β-Yb_5Sb_3-type pnictides (Pn) of the alkaline-earth and dipositive rare-earth metals. The problem was solved with the discovery that all nine examples assigned to the latter structure type were in fact valence hydrides $(A^{II})_5Pn_3H$ (3, 4) in what is better termed the orthorhombic Ca_5Sb_3F structure type (5). This was the first instance in our work in which fluoride, which is easily located by modern X-ray diffraction means,

0022-4596/01 $35.00

was utilized as a good stand-in for hydride, although this relationship has been known for much longer (6). Evidently, the most prevalent sources of hydrogen impurities have been commercial alkaline-earth metals, although most active metals can become contaminated with careless handling. (Hydrogen is commonly retained during their reactions with adventitious water.) Examples in the same Mn_5Si_3-type systems in which the pnictide hydride forms first, or only, by utilizing a well-characterized interstitial hole (7) in that structure type will be described in a forthcoming manuscript (8). Other specific hydride errors have included the Zintl phases $Ba_5Ga_6H_2$ (9) and $Ba_{21}M_2O_5H_{22+x}$ (M = Si, Ge, Ga, etc., $x = 2{,}0$) (10), the structures of which were originally reported without the hydrogen components.

Similar events have shadowed the chemistry of the related A_5Tt_3 phases of the tetrel (Tt) elements Si–Pb. These are frequently encountered with tetragonal Cr_5B_3-type structures with the characteristic equal numbers of monomeric and dimeric anions, meaning that those with divalent cations formally meet the structural criterion (2) for Zintl phases, i.e., $(A^{+2})_5(Tt_2^{-6})(Tt^{-4})$ in terms of oxidation states. One might even imagine that these closed-shell configurations should be immune to oxidation and to the inclusion of hydride without a necessary change of structure type. In fact, the problems here are particularly insidious because not only is oxidation of the substrate by hydrogen generally possible, but the hydride formed is also readily incorporated into a suitable cavity already present in the parent Cr_5B_3 structure. We have recently reported on seven instances with tin or lead for which *only* the stuffed Cr_5B_3 structure type is stable in the new Ca_5Sn_3F structure type (or the hydride equivalent), namely, for the Ca–Sn, Ba–Sn, Eu–Sn, Yb–Sn, Sr–Pb, Ba–Pb and Eu–Pb systems (11). All that were tested also form the corresponding isotypic A_5Tt_3F. Thus, major hydride contamination was evidently the source of ten reports of these particular binary combinations as simple tetragonal $A_5(Tt)_3$ phases. In these systems, the truly binary A_5Tt_3 compositions occur in another structure type or, in one instance, Ba–Sn, that composition exists as a mixture of two other binary phases. In fact, such serious hydride errors had evidently precluded the discovery of the oligomeric $Sr_{31}Pb_{20}$, which has a very similar composition, 60.8 at.% Sr vs 62.5 at.% for Sr_5Pb_3, until 1993 (12).

The present article reports on nine more complicated instances in which *both* the binary and the ternary (hydride) phases occur with the same heavy atom Cr_5B_3 structure type. This situation naturally means that X-ray lattice dimensions are probably the quickest and best way to tell them apart and, in retrospect, usually the only means available. Of course, comparison of dimensional data from different time periods and equipment naturally entails some uncertainties. It should be noted that still six more members of the A_5Tt_3 family, apparently only with A = Sm and Yb, exhibit a Mn_5Si_3 type structure for the binary (usually) as well as for the stuffed version as the hydride, which is another future topic (8).

The presence of a significant tetrahedral cavity in the Cr_5B_3 structure type was first signaled by the serendipitous discovery of a stuffed Cr_5B_3-type structure for La_5Pb_3O (via dirty lead) (13). The lead atoms here are all monomeric in the presence of these electron-richer cations, and the analogous nitride would appear to be electron-precise. (A similar disposition of monoanions is also known in the distinctive so-called In_5Bi_3 subfamily (14).) We choose to distinguish the structure of La_5Pb_3O and its absence of a dimer from the situation in the new Ca_5Sn_3F structure type where the dimeric anion is retained, although both types occur in the same space group and are isopointal.

The protocol developed earlier for studies of the Mn_5Si_3H- vs Ca_5Sb_3F-type phase problems (4) was again applied to test for the formation of hydride derivatives as well as to ensure the absence of impurity hydrogen in checks for the formation of true Cr_5B_3 types and the ternary fluorides. Although it is possible to clean the alkaline-earth metals, etc., aforehand by careful dissociation of hydrogen in vacuum, it is generally far easier to simply load the reactants in tantalum tubing, weld this shut, and heat the assembly in high vacuum at, say, 900–1200°C. The metals and any hydride compounds evidently all have appreciable H_2 dissociation pressures under these conditions, and tantalum is permeable to only hydrogen in our systems above 550–600°C. Subsequent equilibrations of a virtually hydrogen-free system can then be made at suitable temperatures. On the other hand, Ta sample containers loaded with hydrogen sources, e.g., CaH_2, are equilibrated only after their further enclosure in sealed fused silica jackets in order to retain the hydrogen. Additional smaller amounts of hydrogen can still originate from water dissociation from the fused silica over long periods or at higher temperatures. These two routes will hereafter be designated as the dynamic vacuum (dv) and sealed (SiO_2) container (sc) methods.

2. EXPERIMENTAL SECTION

Materials utilized were: Ca, Sr, Ba (Ae) from APL Engineering, distilled and sealed in glass; Eu and Yb, Ames Laboratory $\geq 99.95\%$ total; Si, electronic grade, Ge and Sn, Aesar 5–9's or better. The AH_2 phases were prepared by direct reaction of H_2 with the metals held in a Mo boat within a closed vacuum system that was equipped with a diaphragm manometer. The reactions were run to completion at 420 to 700°C under 600–700 torr H_2, depending on the dissociation characteristics of the particular hydrides (15). All were treated as stoichiometric AH_2 phases, as verified by their cell dimensions (15, 16). The AeF_2 reagents were precipitated from $AeCO_3$ slurries with excess HF(aq), filtered, washed, and vacuum-dried at 400°C.

In particular cases, the as-received alkaline-earth metals were dehydrogenated after sealing them in Ta containers. These were heated in silica tubing under high vacuum ($\leq 10^{-5}$ torr), namely, at 650°C for Ca and at 710°C for the remainder for $\sim$ 12 h or until the vacuum stayed below that producing a Tesla coil discharge after a small increase in temperature.

All reactions between the elements with or without fluoride or hydride were carried out in welded Ta containers that were heated either under vacuum or within evacuated, well-flamed, and sealed silica jackets, depending on the target. All reagents and products were handled in gloveboxes with 0.2–0.4 ppm (vol) H_2O levels. These techniques as well as those for Guinier powder pattern measurements (with NIST Si as an internal standard) and lattice constant least-squares refinement methods have been described in more detail before (4, 17, 18). A Cu$K\alpha_1$ wavelength of 1.54056 Å was used for this purpose. The phase distributions in mixed products were estimated in terms of equivalent X-ray scattering powers in their powder patterns with the aid of calculated patterns for known phases. Although the accuracies of these estimates vary perhaps by $\pm$ 2–5%, they are internally more precise then that. All phases seen are reported. Single crystals of eight of the compounds reported here were selected under low magnification and mounted in thin-walled glass capillaries in a glovebox for X-ray diffraction. These were first checked for quality with Laue photographs. The data collection and refinement parameters are detailed in Table 1. Absorption was corrected for with the aid of three psi-scans collected at $\chi \geq 80°$ and, after isotropic refinement, with DIFABS except for Ca_5Ge_3. Structural refinements were made with the TEXSAN (19) package. Lattice dimensions secured from calibrated Guinier powder pattern data were used in all distance calculations from single-crystal results. The F_o/F_c listings are available from J.D.C.

Magnetic susceptibility data were secured for seven single-phase weighed samples, each held between two fused silica rods that fit snugly inside a 5-mm o.d. tube in a container sealed under He. The measurements were made with the aid of a Quantum Design MPMS SQUID magnetometer at 3 T and between 6 and 300 K. The data were corrected for the susceptibilities of both the apparatus and the atomic cores in the sample. Resistivities of two phases were measured by the Q-method at $\sim$ 35 MHz on an improved apparatus (20).

3. RESULTS AND DISCUSSION

3.1. Syntheses

Table 2 lists conditions of 22 representative reactions run for these systems, the products identified from by powder patterns, and the Guinier lattice constants of the tetragonal Cr_5B_3-type phases obtained (34). Dimensional data are also given from 14 literature reports of these as binary phases. All in this group have the particular problem that each system contains both a binary A_5Tt_3 and a ternary $A_5Tt_3H_x$ with the same heavy atom structure, namely for, Ca, Sr, Ba, Eu with either Si or Ge, plus Sr–Sn. Hydride formation can be best judged on a routine basis by the customary decrease in cell dimensions and volumes (0.3 to 2%) following the reaction of a $A_5Tt_3H_{2.0}$ composition in a sealed container relative to those for Ae_5Tt_3 binary phases synthesized under dynamic vacuum conditions to ensure the absence of significant hydrogen. Furthermore, all of those tested, Ca_5Si_3, Ba_5Si_3, and Ca_5Ge_3, also form the characteristic fluoride $A_5Tt_3F_x$ (dv), and their fluoride contents have all been quantified by single crystal X-ray diffraction studies.

This condition is not true for the hydrides for which their hydrogen contents were not quantified. The magnitudes of the hydrogen dissociation pressures are unavailable in all cases, either at 650°C, the final temperature of the equilibrations, or at some higher temperature should the uptake rate become insignificant relative to a cooling rate of 10°C/h. (Substantially full hydrogen occupancy in Ca_5Sn_3D was established earlier from a neutron diffraction study (11).) Of course, a parallel uncertainly also exists with regard to the rate of change of cell dimensions with variation of the hydrogen content. Assessments as to whether, by comparison, earlier reports of the supposedly binary A_5Tt_3 phases were troubled by unrecognized hydrogen impurities are also naturally dependent on the accuracies of the earlier data, whatever the diffraction technique. But earlier studies of both the Cr_5B_3-type A_5Tt_3 (11) and "β-Yb_5Sb_3-type" A_5Pn_3 (4) systems in which *only* the ternary hydrides are stable suggest that contamination has been pervasive. Of course, the occurrence of a negative result in a really hydrogen-free system of this latter type is virtually impossible to assess unless a phase diagram is reported or a virtually quantitative yield of another product is obtained. We also assume that a continuous variation of dimensions occurs in the present single phase A_5Tt_3–$A_5Tt_3H_x$ systems because we have never seen otherwise.

3.2. Results

3.2.1. Silicides. The A_5Si_3 phases for A = Ca, Sr, Ba, Eu all form $A_5Si_3H_x$ hydrides from loaded compositions $A_5Si_3H_{2.0}$ when first reacted (sc) at 1100°C and then slowly cooled to 650°C (conditions in Table 2). We assume $x \leq 1.0$ because of structural limitations (below). In order to get good yields for binary Ca–Si and Sr–Si and ternary Ca–Si–F compositions, we found it necessary to heat these first to 1300°C, near the melting points, before slow cooling to 600°C. This follows our earlier discovery that reactions to form Ca_5Sb_3F and Ca_5Bi_3F from the elements and CaF_2 were very incomplete when carried out at 900°C, even

TABLE 1
Data Collection and Refinement Parameters

	Ca_5Si_3	$Ca_5Si_3F_{0.42}$	Sr_5Si_3	$Ba_5Si_3F_{0.16}$
Space group	*I*4/*mcm* (No. 140)	*I*4/*mcm*	*I*4/*mcm*	*P*4/*ncc* (No. 130)
Density calculations (g/cm^3)[a]	2.178	2.333	3.368	4.445
Crystal dimensions (mm)	$0.12 \times 0.20 \times 0.32$	$0.16 \times 0.30 \times 0.36$	$0.15 \times 0.18 \times 0.26$	$0.12 \times 0.25 \times 0.30$
Diffractometer	Enraf–Nonius CAD4	Enraf–Nonius CAD4	Enraf–Nonius CAD4	Enraf–Nonius CAD4
Collected octants	$h, -k, \pm l$	$-h, -k, \pm l$	$-h, -k, \pm l$	$h, -k, \pm l$
Scan type	$\omega - 2\theta$	$\omega - 2\theta$	$\omega - 2\theta$	$\omega - 2\theta$
2θ limit (deg.)	54	54	54	54
Absorption coefficient (cm^{-1})	33.3	33.7	252.2	167.0
Rel. transm. coeff. range	0.833–1.00	0.797–1.00	0.697–1.00	0.752–1.00
Number of reflections				
Meas. (obs.[b])	2182 (837)	2173 (812)	2571 (744)	2898 (1893)
Indep. (obs.[b])	700 (275)	807 (299)	937 (287)	1115 (673)
R_{ave}(%)[b]	5.55	7.79	15.8 (7.85[c])	9.75
No. of refined variables	16	21	16	23
R/R_w (%)[d]	1.5/1.9	2.5/2.6	3.5/3.7	3.2/3.6
Goodness of fit	1.120	0.946	1.166	1.927
Sec. extinc. coeff. (10^{-8})	11.6(9)	14(2)	4.5(7)	6.7(4)
Max./min. in ΔF map (e$^-$ Å^{-3})	0.25/ −0.26	0.43/ −0.42	1.35/ −1.21	0.240/ −1.03
	$Eu_5Si_3H_x$	Ca_5Ge_3	$Ca_5Ge_3H_x$	$Ca_5Ge_3F_{0.66}$
Space group	*I*4/*mcm*	*I*4/*mcm*	*I*4/*mcm*	*I*4/*mcm*
Density calculations (g/cm^3)[a]	5.887	3.134	3.185	3.303
Crystal dimensions (mm)	$0.18 \times 0.24 \times 0.32$	$0.11 \times 0.16 \times 0.22$	$0.16 \times 0.22 \times 0.25$	$0.17 \times 0.20 \times 0.28$
Diffractometer	Enraf–Nonius CAD4	Enraf–Nonius CAD4	Enraf–Nonius CAD4	Enraf–Nonius CAD4
Collected octants	$-h, -k, \pm l$	$h, k, \pm l$	$h, k, \pm l$	$h, \pm k \pm l$
Scan type	$\omega - 2\theta$	$\omega - 2\theta$	$\omega - \theta$	$\omega - 2\theta$
2θ limit (deg.)	54	56	56	56
Absorption coefficient (cm^{-1})	327.1	127.2	129.0	128.5
Rel. transm. coeff. range	0.673–1.00	0.546–1.00	0.661–1.00	0.761–1.00
Number of reflections				
Meas. (obs.[b])	2164 (828)	2443 (817)	2397 (849)	3104 (1176)
Indep. (obs.[b])	821 (301)	824 (281)	1184 (430)	832 (321)
R_{ave}(%)[b]	4.30	6.70	7.23	10.9
No. of refined variables	16	16	16	21
R/R_w (%)[d]	2.1/2.4	1.9/2.2	2.9/3.0	2.1/2.4
Goodness of fit	1.926	1.171	1.527	0.981
Sec. extinc. coeff. (10^{-8})	7.4(2)	4.0(5)	1.3(6)	9(1)
Max./min. in ΔF map (e$^-$ Å^{-3})	1.10/ −1.08	0.67/ −0.59	0.94/ −0.75	0.62/ −0.88

[a]Lattice parameters obtained from calibrated Guinier powder pattern data are in Table 2.
[b]All data $I > 0$.
[c]Observed reflections; $I \geq 3\sigma_I$.
[d]$R = \sum||F_o| - |F_c||/\sum|F_o|$; $R_w = [\sum w(|F_o| - |F_c|)^2/\sum w(F_o)^2]^{1/2}$; $w = \sigma_F^{-2}$.

though a liquid phase is in equilibrium with Ca_5Sb_3(s) (incongr. m.p. $\sim$ 996°C) for the former (35), whereas a few hours at 1250°C was much more effective (5). Lattice constants given in the 1974 report of Ca_5Si_3 (21) (Table 2), if accurate, indicate a substantial hydride impurity was present, whereas the very recent report on the Ca–Si phase diagram by Manfrinetti and coworkers (22) gave Guinier-based lattice constants that are in good agreement with ours. This probably happened because their thermal analysis samples were sealed in Ta and first melted (> 1240°C) through induction heating, which should have removed any hydrogen. The single-crystal X-ray diffraction results for Ca_5Si_3 and $Ca_5Si_3F_{0.4}$ will be described later.

Analogous results pertain to Sr_5Si_3 and $Sr_5Si_3H_{2.0}$ compositions treated under dv and sc conditions, respectively, Table 2. The cell volume from the 1967 report of the binary

TABLE 2
Reaction and Lattice Data for A_5Tt_3 Phases with Cr_5B_3-Type Structures that Are Stable as Binary as well as Ternary Hydrides and Fluorides

		Approximate yields, %[b]		Lattice parameters of the Cr_5B_3-type phase (Å,Å^3)			
Loaded	Condition[a]	C	Other	*a*	*c*	*V*	*a*/*c*
Ca_5Si_3	dv 1	90	10 CS	7.6495(4)	14.835(2)	868.1(1)	0.516
$Ca_5Si_3H_{2.0}$	sc 2	> 95		7.6386(3)	14.747(1)	860.5(1)	0.518
Ca_5Si_3F	dv 1	75	10CS, 15CaF_2	7.6354(4)	14.829(2)	864.5(1)	0.515
Ref. (21)				7.64	14.62	853	
Ref. (22)				7.641(1)	14.876(2)	868.5	0.514
Sr_5Si_3	dv 1	95	un	8.0966(5)	15.703(2)	1029.9(2)	0.516
$Sr_5Si_3H_{2.0}$	sc 2	~ 100		8.0468(4)	15.761(1)	1020.5(1)	0.510
Ref. (23)[c]				8.055	15.688	1017.9	0.513
Ref. (24)				8.089(4)	15.733(8)	1029 (1)	0.514
Ba_5Si_3[c]	dv 2	90 (B)	un	8.4855(6)	16.421(3)	1182.4(3)	0.517
$Ba_5Si_3H_{2.0}$	sc 2	> 95 (B)		8.4558(4)	16.484(2)	1178.6(1)	0.513
Ba_5Si_3F	dv 1	80 (B)	15BaF_2, un	8.4726(2)	16.443(1)	1180.3(1)	0.515
Ref. (25)				8.436(6)	16.53(1)	1176 (1)	0.510
Ref. (26)				8.465(6)	16.45(1)	1179 (1)	0.515
Eu_5Si_3	dv 3	40	20M, un	7.919(2)	15.384(6)	964.9(5)	0.515
$Eu_5Si_3H_{2.0}$	sc 2	95		7.9052(4)	15.281(2)	954.9(1)	0.517
Ref. (27)				7.9188(7)	15.322(2)	960.8(2)	
Ca_5Ge_3	dv 2	95	5CB	7.7156(5)	14.885(2)	886.1(1)	0.518
$Ca_5Ge_3H_{2.0}$	sc 2	~ 100		7.7218(5)	14.660(2)	874.2(1)	0.527
$Ca_5Ge_3F_{1.0}$	dv 3	> 90	5CB, < 5 CaF_2	7.7093(3)	14.789(2)	879.0(1)	0.521
$Ca_5Ge_3F_{1.5}$	dv 2	60	30CB, 10CaF_2	7.7101(3)	14.787(2)	879.0(1)	0.521
Ref. (21)				7.74	14.66	878	
Sr_5Ge_3	dv 2	95	5CB	8.1675(4)	15.730(3)	1049.3(1)	0.519
$Sr_5Ge_3H_{2.0}$	sc 2	~ 100		8.1236(5)	15.732(2)	1038.2(2)	0.516
Ref. (28)				8.134(4)	15.771(8)	1043 (1)	0.516
Ba_5Ge_3	dv 2	> 95 (B)		8.557(1)	16.465(1)	1205.6(4)	0.520
$Ba_5Ge_3H_{2.0}$	sc 2	95 (B)	5CB	8.5106(5)	16.549(2)	1198.7(2)	0.514
Ref. (29)				8.519(4)	16.554(8)	1201 (1)	0.515
Eu_5Ge_3	dv 2	90	10CB	7.9987(8)	15.380(3)	984.0(2)	0.520
$Eu_5Ge_3H_{2.0}$	sc 2	~ 100		7.9853(5)	15.281(2)	974.4(1)	0.522
Ref. (30)				7.990(1)	15.367(1)	981.0(1)	0.520
Sr_5Sn_3	dv 2	> 95		8.5757(8)	16.318(2)	1200.1(2)	0.525
$Sr_5Sn_3H_{2.0}$	sc 2	95	5CB	8.5694(5)	16.027(3)	1176.9(2)	0.535
Ref. (31)				8.54(1)	16.06(2)	1171 (3)	0.532
Ref. (32)				8.565	16.261	1192.9	0.527
Ref. (33)				8.567(2)	16.254(7)	1192.9(8)	0.527

[a] Conditions: dv = dynamic vacuum, sc = sealed silica jacket; 1: 1300°C for 6 h, 8°C/h to 600°C, cool; 2: 1150°C for 6 h, 10–12°C/h to 650°C; 3: 1200°C for 6 h, 20°C/h to 1100°C, 6 h, 10°C/h to 600°C.

[b] Structural types: C, Cr_5B_3; CS, Co_2Si; B, Ba_5Si_3 distortion of Cr_5B_3; CB, orthorh. CrB; CS, Co_2Si; M, Mn_5Si_3.

[c] Reduced symmetry.

(23) clearly pertained to the hydride, again, if the data were accurate. Although the cell volume from a 1999 single-crystal report for Sr_5Si_3 (24) agrees closely with ours for the binary phase, the cell in fact reapportions appreciably on hydrogen uptake, and their individual cell dimensions (refined from multiple diffractometer data) put their sample into the probable hydride region. A comparison of the positional data (below) make this categorization more certain.

The Ba_5Si_3 compound is well known for its primitive distortion of the Cr_5B_3-type parent (abbreviated B in the table) (25), as will be described later for the comparable

$Ba_5Si_3F_x$. This is another case in which the lattice constants move in opposite directions on hydrogen uptake. The lattice constants from both the 1966 (25) and the 1999 (26) studies at face value indicate appreciable hydrogen contamination.

What was new at the time, Eu_5Si_3 (34), also forms a hydride with a 1.0% volume contraction. The recently reported single-crystal study of Eu_5Si_3 (27) may have involved some hydrogen although their (Guinier) lattice constants

TABLE 3
Refined Positional and Displacement Parameters for $Ca_5Tt_3(H,F)_x$ Phases with Cr_5Sn_3F-Type Structures

Atom[a]	x	y	z	B_{eq}(Å^2)	U^b_{11}	U_{22}	U_{33}	U_{12}	U_{13}	U_{23}
Ca_5Si_3										
Ca1	0	0	0	1.27(2)	0.0108(3)	U_{11}	0.0267(4)	0	0	0
Ca2	0.17978(3)	$x+\frac{1}{2}$	0.13986(2)	1.00(2)	0.0141(2)	U_{11}	0.0099(2)	−0.0008(1)	−0.0005(1)	U_{13}
Si1	0	0	$\frac{1}{4}$	1.13(2)	0.0147(3)	U_{11}	0.0134(5)	0	0	0
Si2	0.38693(6)	$x+\frac{1}{2}$	0	0.83(2)	0.0109(2)	U_{11}	0.0097(3)	−0.0005(2)	0	0
$Ca_5Si_3F_{0.4}$										
Ca1	0	0	0	1.64(3)	0.0127(4)	U_{11}	0.0371(7)	0	0	0
Ca2	0.17407(5)	$x+\frac{1}{2}$	0.14386(3)	1.34(2)	0.0178(3)	U_{11}	0.0153(3)	0.0017(2)	−0.0039(1)	U_{13}
Si1	0	0	$\frac{1}{4}$	1.27(3)	0.0167(6)	U_{11}	0.0150(7)	0	0	0
Si2	0.38724(8)	$x+\frac{1}{2}$	0	0.88(2)	0.0119(3)	U_{11}	0.0096(4)	0.0006(3)	0	0
F[c]	0	$\frac{1}{2}$	$\frac{1}{4}$	0.9(1)	0.015(2)	U_{11}	0.005(3)	0	0	0
Sr_5Si_3										
Sr1	0	0	0	1.27(5)	0.0077(7)	U_{11}	0.033(1)	0	0	0
Sr2	0.18003(7)	$x+\frac{1}{2}$	0.14008(6)	0.74(2)	0.0106(4)	U_{11}	0.0070(5)	−0.0014(3)	−0.0010(3)	U_{13}
Si1	0	0	$\frac{1}{4}$	1.0(1)	0.013(2)	U_{11}	0.013(3)	0	0	0
Si2	0.3920(3)	$x+\frac{1}{2}$	0	0.59(9)	0.008(1)	U_{11}	0.006(2)	−0.000(1)	0	0
$Ba_5Si_3F_{0.2}$[d]										
Ba1	$\frac{1}{4}$	$\frac{1}{4}$	0.2716(1)	2.11(3)	0.0203(3)	U_{11}	0.0394(8)	0	0	0
Ba2	0.56191(5)	0.08065(5)	0.10612(3)	1.42(3)	0.0206(3)	0.0187(3)	0.0147(4)	−0.0008(2)	0.0046(2)	−0.0043(3)
Si1	$\frac{1}{4}$	$\frac{1}{4}$	0.4915(3)	1.4(1)	0.020(1)	U_{11}	0.013(3)	0	0	0
Si2	0.6481(2)	$-x$	$\frac{1}{4}$	1.00(6)	0.0157(8)	U_{11}	0.007(2)	0.002(1)	−0.0011(9)	U_{13}
F	3/4	$\frac{1}{4}$	0	0.8(5)						
$Eu_5Si_3H_x$										
Eu1	0	0	0	1.98(3)	0.0134(4)	U_{11}	0.0485(8)	0	0	0
Eu2	0.17414(4)	$x+\frac{1}{2}$	0.14786(3)	1.09(2)	0.0157(3)	U_{11}	0.0099(3)	−0.0001(2)	−0.0024(1)	U_{13}
Si1	0	0	$\frac{1}{4}$	1.1(1)	0.015(1)	U_{11}	0.011(3)	0	0	0
Si2	0.3925(3)	$x+\frac{1}{2}$	0	0.86(8)	0.012(1)	U_{11}	0.008(2)	0.001(1)	0	0
(H	0	$\frac{1}{2}$	$\frac{1}{4}$)							
Ca_5Ge_3										
Ca1	0	0	0	1.18(4)	0.0079(5)	U_{11}	0.029(1)	0	0	0
Ca2	0.17807(8)	$x+\frac{1}{2}$	0.13998(6)	0.95(2)	0.0122(3)	U_{11}	0.0117(4)	−0.0008(3)	−0.0006(2)	U_{13}
Ge1	0	0	$\frac{1}{4}$	1.04(2)	0.0124(3)	U_{11}	0.0148(5)	0	0	0
Ge2	0.38200(6)	$x+\frac{1}{2}$	0	0.70(1)	0.0074(2)	U_{11}	0.0117(3)	−0.0004(3)	0	0
$Ca_5Ge_3(H_x)$										
Ca1	0	0	0	1.50(5)	0.0116(6)	U_{11}	0.034(1)	0	0	0
Ca2	0.16797(8)	$x+\frac{1}{2}$	0.14852(8)	1.09(2)	0.0153(3)	U_{11}	0.0108(6)	−0.0001(3)	−0.0018(3)	U_{13}
Ge1	0	0	$\frac{1}{4}$	1.08(3)	0.0136(3)	U_{11}	0.0139(6)	0	0	0
Ge2	0.38296(6)	$x+\frac{1}{2}$	0	0.85(2)	0.0114(3)	U_{11}	0.0096(4)	−0.0004(3)	0	0
(H	0	$\frac{1}{2}$	$\frac{1}{4}$)							
$Ca_5Ge_3F_{0.7}$										
Ca1	0	0	0	1.69(4)	0.0118(6)	U_{11}	0.041(1)	0	0	0
Ca2	0.16964(7)	$x+\frac{1}{2}$	0.14617(5)	1.26(2)	0.0167(3)	U_{11}	0.0146(4)	0.0013(3)	−0.0036(2)	U_{13}
Ge1	0	0	$\frac{1}{4}$	1.16(2)	0.0151(3)	U_{11}	0.0138(4)	0	0	0
Ge2	0.38224(4)	$x+\frac{1}{2}$	0	0.81(1)	0.0108(2)	U_{11}	0.0091(3)	0.0002(2)	0	0
F[e]	0	$\frac{1}{2}$	$\frac{1}{4}$	1.4(2)	0.020(3)	U_{11}	0.013(3)	0	0	0

[a] Wyckoff positions for Ca1, Ca2, Si1, Si2, and F atom positions are 4*c*, 16*l*, 4*a*, 8*h* and 4*b*, respectively, and site symmetries for the same atoms are 4/*m*, ..*m*, 422, *m*2*m* and $\bar{4}2m$, respectively.

[b] $T = \exp[-2\pi^2(U_{11}h^2a^{*2} + U_{22}k^2b^{*2} + U_{33}l^2c^{*2} + 2U_{12}hka^*b^* + 2U_{13}hla^*c^* + 2U_{23}klb^*c^*)]$.

[c] Occupancy = 0.42(1).

[d] $P4/ncc$, origin at $\bar{1}$. Occupancy of F = 0.16(2).

[e] Occupancy = 0.66(2).

inexplicably differ from ours only in *c*, which shows 60% of the contraction we observe on hydride formation.

3.2.2. Germanides. The Ca–Ge system likewise contains the binary Ca_5Ge_3 as well as the stuffed hydride and fluoride. The cell volume from the 1974 report (21) on Ca_5Ge_3 suggests some hydride, but the values are probably not accurate enough for that judgement. A second fluoride reaction loaded as $Ca_5Ge_3F_{1.5}$ yielded the same product (except for excess CaF_2) as for $Ca_5Ge_3F_{1.0}$ according to the two sets of lattice data. This indicates that equilibrium had been attained at the upper limit of fluoride, which was refined to have an occupancy of ~ 0.66 (below).

The germanides Sr_5Ge_3, Ba_5Ge_3, and Eu_5Ge_3 also show clear differentiation from the respective ternary hydrides according to our experiments. The recently reported *c* dimension for the Sr_5Ge_3 (28) falls outside of the range we observed, and so the comparison is inconclusive. Comparison of dimensions reported for Ba_5Ge_3 (29) (from multiple diffractrometer data) indicate a substantial hydrogen involvement, and for Eu_5Ge_3 with Guinier data (30), possibly but not seriously so. The Ba_5Ge_3 and its hydride both occur with distorted Ba_5Si_3 type (*P*4/*ncc*) structures according to both our powder data and a single-crystal study of the former (29).

3.2.3. Stannide. Finally, Sr_5Sn_3, which evidently is the only stannide or plumbide that forms both a binary and a ternary hydride with the same structure, has been reported three times before. The first in 1977 (31) had clear hydrogen involvement, whereas the 1978 report (32) was possibly so troubled, judging solely from the dimensions; however, four other 5:3 products described in the same article are known to have been uniquely hydrogen-stabilized (4, 8, 11). The 1994 result from our labs (33), synthesized from Sr metal from the same source without any special cleaning, appears to have been roughly one-third saturated. As an aside, we have also shown that none of the 3*d* elements V–Ni introduced as potential interstitials afford any alternative to the Cr_5B_3-type binary product. The search for a possible stuffed Mn_5Si_3-type Sr_5Sn_3M was predicated on the formation of this sort of product for Ca_5Pb_3M (36).

3.3. Structures

The structures of eight of the compounds reported here were refined with the aid of single-crystal X-ray diffraction data. General collection and refinement parameters were given in Table 1. Table 3 contains the atomic positional and displacement ellipsoid data, and Tables 4 and 5 list important distances in these. Seven occur as the classical or the stuffed Cr_5B_3 (Ca_5Sn_3F) structure type (*I*4/*mcm*), whereas the eighth, $Ba_5Si_3F_{0.2}$, exhibits the characteristically distorted structure known for its parent Ba_5Si_3 (*P*4/*ncc*) (25).

The stuffed Cr_5B_3-type tetragonal structure is illustrated for the $Ca_5Ge_3F_{0.6}$ example in Fig. 1. The structure type has two characteristic features: (i) the equal distribution of main-group tetrel anions (solid spheres) between monomers (in layers at $z = \frac{1}{4}$ and $\frac{3}{4}$) and dimers (in the mirror planes at $z = 0, \frac{1}{2}$), each with different orientations in its repeat (i.e., from centering and the mirror plane at $z = \frac{1}{2}$); (ii) interstitial tetrahedral cavities defined by Ca2 atoms (shaded) around $(0, \frac{1}{2}, \frac{1}{4})$, $(0, \frac{1}{2}, \frac{3}{4})$, etc. which may be occupied by H, F, or nothing. These two features are also shown in normal views looking in $\vec{c}$ in Fig. 2: (a) the section around $z = \frac{1}{2}$ that

TABLE 4
Important Interatomic Distances (Å) in Cr_5B_3-like Structures

Atom 1–Atom 2	Ca_5Si_3	$Ca_5Si_3F_{0.4}$	Ca_5Ge_3	$Ca_5Ge_3H_x$	$Ca_5Ge_3F_{0.6}$	Sr_5Si_3	$Eu_5Si_3H_x$
Tt2–Tt2 1×	2.447(1)	2.435(2)	2.575(1)	2.556(1)	2.5678(9)	2.474(7)	2.403(7)
*Tt*1–*A*1 2×	3.7088(5)	3.7073(5)	3.7213(5)	3.6650(5)	3.6972(5)	3.9267(3)	3.8203(3)
*Tt*1–*A*2 8×	3.2498(3)	3.2306(3)	3.2771(5)	3.2356(6)	3.2488(4)	3.276(3)	3.217(2)
*Tt*2–*A*1 2×	3.0836(3)	3.0795(5)	3.0848(4)	3.0922(4)	3.0835(2)	3.4380(5)	3.3116(3)
*Tt*2–*A*2 2×	3.0539(6)	3.1383(9)	3.048(1)	3.202(1)	3.1695(9)	3.293(2)	3.327(3)
*Tt*2–*A*2 4×	3.0957(5)	3.0930(6)	3.1264(8)	3.121(1)	3.1212(7)	3.249(2)	3.215(1)
*A*1–*A*2 8×	3.4923(3)	3.5370(4)	3.5212(6)	3.6050(8)	3.5875(5)	3.6987(6)	3.6947(4)
*A*2–*A*2 1×[a]	3.6039(8)	3.549(1)	3.632(2)	3.473(2)	3.536(1)	3.807(2)	3.553(1)
*A*2–*A*2 1×[b]	3.8897(7)	3.759(1)	3.886(2)	3.669(2)	3.699(2)	4.124(2)	3.894(1)
*A*2–*A*2 1×[c]	4.149(1)	4.267(1)	4.167(2)	4.355(2)	4.323(2)	4.401(2)	4.519(1)
*A*2–*A*2 2×[d]	4.2714(7)	4.120(1)	4.275(2)	3.947(2)	4.034(1)	4.519(2)	4.1622(9)
*A*2–*A*2 4×	3.9728(2)	3.9899(3)	4.0143(4)	4.0634(5)	4.0489(4)	4.2046(4)	4.1306(3)
*A*2–*Z*	(2.540)[e]	2.4516(5)	(2.600)[e]	(2.362)[e]	2.4038(8)	(2.688)[e]	(2.4952)[e]

[a] Unshared side of $(A2)_8$.
[b] Top of tetrahedron = top across $(Tt2)_2$ (viewed along $\vec{c}$).
[c] Height of trigonal prism.
[d] Side of tetrahedron.
[e] To centroid of tetrahedron.

TABLE 5
Important Distances (Å) in $Ba_5Si_3F_{0.2}$

Atom 1–Atom 2		Atom 1–Atom 2	
Si2–Si2	2.442(6)	Ba1–Ba2 4×	3.7991(9)
Si1–Ba1	3.617(5)	Ba1–Ba2 4×	4.055(1)
Si1–Ba1	4.606(5)	Ba2–Ba2[b]	3.892(1)
Si1–Ba2 4×	3.549(3)	Ba2–Ba2[c]	4.2887(9)
Si1–Ba2 4×	3.601(2)	Ba2–Ba2[c] 2×	4.623(1)
Si2–Ba1 2×	3.500(1)	Ba2–Ba2[d] 2×	4.2526(6)
Si2–Ba2[a] 2×	3.378(1)	Ba2–Ba2[d] 2×	4.558(1)
Si2–Ba2[a] 2×	3.458(1)	Ba2–F	2.7646(5)
Si2–Ba2 2×	3.538(2)		

[a]About waist of dimer.
[b]Unshared edge of $(Ba2)_8$.
[c]Ba_4F tetrahedron.
[d]Within squares.

contains the Ge2 dimers (black) (one site is highlighted) and both Ca1 and Ca2 atoms, and (b) the section around $z = \frac{1}{4}$ with the isolated Ge1 atoms, Ca2, and the shaded tetrahedral holes that bind H or F. Note that the squares of Ca2 atoms at the corners and center in each view are common to both parts, square prisms centered by Ca1 at the top and distorted square antiprisms centered by Ge1 in the bottom illustration. The same is true for the top and bottom edges of the $(Ca2)_2$ tetrahedra in (b) and the edges above and below the waist of the dimers in (a).

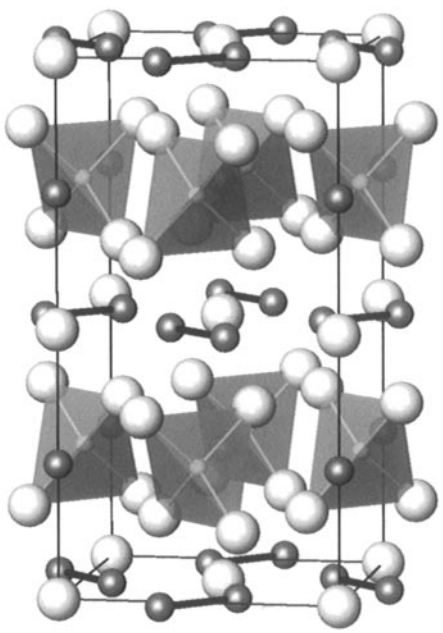

FIG. 1. An off-[100] view of the centered tetragonal structure of $Ca_5Ge_3F_{0.66}$ with vertical. The smaller open and larger solid spheres represent Ca and Ge, respectively, and the interstitial F is centered in the shaded $(Ca2)_4$ tetrahedra.

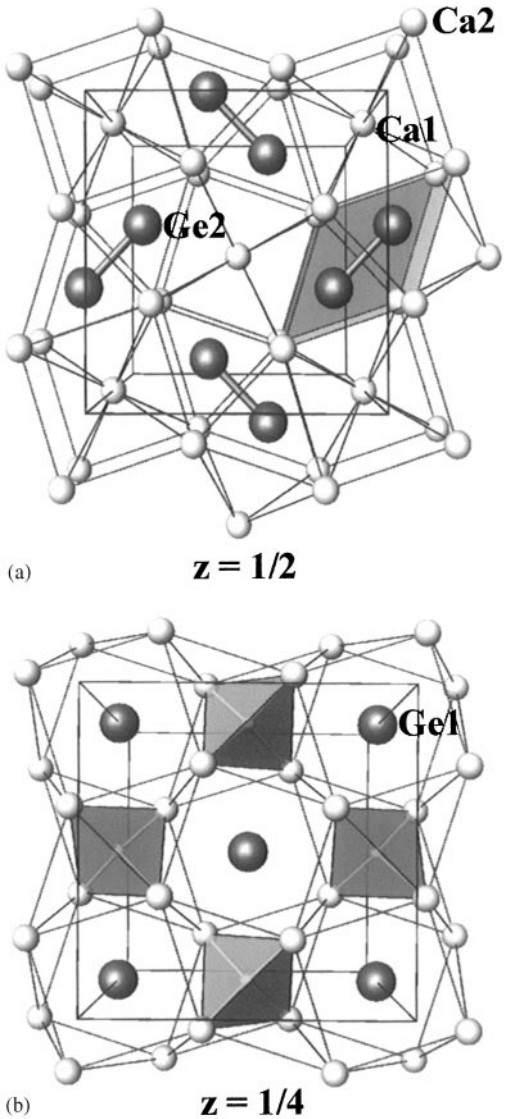

FIG. 2. [001] sections in the $Ca_5Ge_3F_{0.66}$ (Ca_5Sn_3F-type) structure — compare with Fig. 1. (a) the slab centered at $z = 0.5$ (and at $z = 0$ with an altered orientation) with a pair of trigonal prisms surrounding one dimer highlighted; (b) the slab centered at $z = \frac{1}{4}$ with the characteristic Ca2 tetrahedra surrounding fluoride shaded. The atom legends are the same as in Fig. 1.

Compounds in this structural family that have small anions and large cations exhibit a characteristic distortion to the primitive Ba_5Si_3 type structure, $P4/mcc$ (25). These versions have recently been refined for $Ba_5Si_3(H)$ and $Ba_5Ge_3(H)$ (26, 29), whereas we saw the characteristic powder pattern changes for both the two binaries and their hydrides and refined the structure of $Ba_5Si_3F_{0.2}$. The last is illustrated in Fig. 3 around the former 0,0,z axis, Fig. 1. (The structure change includes an origin shift of $\frac{1}{4}, \frac{1}{4}, \frac{1}{4}$.) The typical distortion in this case displaces both Ba1 and Si1 by $+0.355(2)$ and $-0.140(5)$ Å out of the former respective

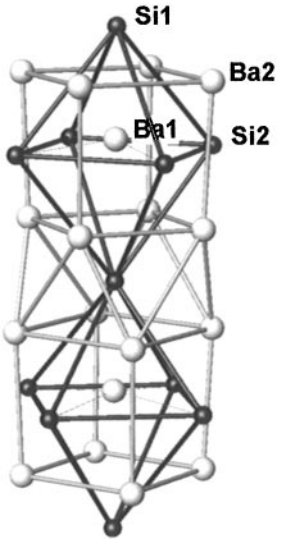

FIG. 3. A portion of the primitive tetragonal cell of $Ba_5Si_3F_{0.16}$ about $\frac{1}{4}, \frac{1}{4}, z$ that shows the characteristic displacements of Ba1 and Si1 from the centers of the former square prismatic and antiprismatic sites defined by Ba2, respectively.

planes at $z = 0$ and $\frac{1}{4}$. As noted before (26), this likely occurs because of crowding in the once-Ba1-centered square prism, which distortion now makes the faces of the prism of unequal size (Table 5). The proportions of the F-centered tetrahedron as well as separations in $(Tt2)_2$ remain typical, both sites being relatively well removed from the distortion sites.

Binding of H or F in the nominal tetrahedra ($\bar{4}2m$) always produces a contraction of the tetrahedral site and the lattice (Table 6), evidence of the additional bonding therein. The gain from this is presumably responsible for tipping the scales of stability for the group of stannide and plumbide examples reported earlier that exist only as ternary hydride and fluoride phases. The sole instance in which a comparison of atom positions from published single crystal studies with ours is useful are those for Sr_5Si_3 (24). Although the cell dimension alone suggests probable hydrogen contamination, the fractional coordinates establish this more clearly. Those for Sr2, which define the tetrahedra, show the principal differences, as would be expected on examination of all aspects of the structure (the variables for Si2 differ by $< 1\sigma$ while the other atom types lie in fixed positions). The reported x and z coordinates of Sr2 differ from ours by -0.00188 (24σ) and $+0.00154$ (23σ), differences that are 18.6 and 18.0% of the characteristic shifts observed in single crystal data for Ca_5Ge_3H relative to Ca_5Ge_3 (Table 3). This shift makes d(Sr2-centroid) 0.031 Å smaller than in the present binary. (The results for $Sr_{5-x}Ca_xSi_3$, $x = 0.38$, 0.48, and $Sr_5Si_{2.87}Ge_{0.13}$ (37) are similar but the last is not quite as extreme. The reverse analysis, $Eu_5Si_3H_x$ vs Eu_5Si_3 (27), is not as clear.) Both studies agree that the distorted structure ($I4cm$) attributed to Sr_5Si_3 in 1967 (23) was not attained.

TABLE 6
Observed Cell Volume Decrements (%) between A_5Tt_3 and $A_5Tt_3H_x$[a] or $A_5Tt_3F_x$[b]

$A\backslash Tt$	Si	Ge	Sn
Ca	0.88	1.36	
	0.42	0.81	
Sr	0.92	1.07	1.97
Ba	0.32[c]	0.59[c]	
	0.18[c]		
Eu	1.05	0.98	

[a]All loaded as $A_5Tt_3H_{2.0}$ and equilibrated down to 650°C.
[b]Cr_5B_3- and Ca_5Sn_3F-type structures. The fluoride differences are on the second line.
[c]Ba_5Si_3-type.

The three refined fluoride occupancies, 0.42, 0.66, 0.16 in the Ca–Si, Ca–Ge, and Ba–Si systems, respectively, are unusual in their contrast, although the cell volume decrements in forming these from the clean binary components are reasonably proportional to fluoride content. All were achieved from $A_5Tt_3F_{1.0}$ loadings, but the same result was attained for $Ca_5Ge_3F_{1.5}$ (Table 2), so equilibrium appears to have been attained. Our earlier article also reported on the structures of $Ca_5Sn_3F_{0.89(1)}$ and $Sr_5Pb_3F_{1.0}$ in systems in which the binary version does not exist. The best proposition, lacking more information, is that these five fluorine coefficients represent the compositions in equilibrium with AF_2(s) (plus, presumably, small amounts of other phases). The coefficients generally increase with the size, and presumed reduced bond strengths, of the heavier tetrelide dimers. In addition, the interstitials are second-nearest neighbors (through $A2$) to, and would with increasing concentration withdraw more π^* electron density from the heavier weaker dimers (below).

3.4. Structural Generalizations

Some characteristic and significant distances and their differences are summarized in Table 7 for the 12 A_5Tt_3Z compounds we have structurally refined in this work or before (11). Although variations among the two or three different elements that make up the structures could result in some substantial and complex relationships among them, the results are remarkable for the regularities that can be found among them. Distances in the tetrel dimers are quite consistent within each type. These are 2.40–2.47 Å among four silicides with three cations, and 2.56–2.58 Å for three germanides with the same Ca cation, with or without H or F (Table 7, col. **1**). The dimers in the three stannides are likewise more similar in length, 2.88–2.91 Å, than might be expected for the cation and interstitial variations. But, the dimer distances found with europium with tin or silicon are

TABLE 7
Some Important Distance Parameters (Å) in $A_5Tt_3(Z)$ Phases with Refined Structures

	(1) d(Tt–Tt)	(2) Matrix effect on dimer: $\Delta d(Tt2$–A2), end–waist	(3) Matrix effect on dimer: $\Delta d(A2$–$A2)$ side-top	(4) Tetrah. radius, $A2$–Z	(5) Side/top proportion in tetrah.	(6) Top edge of tetrah.	(7) Twist in $(A2)_8$: unshared– shared side edges	(8) Square: $d(A2$–$A2)$ $(4\times)$	(9) Radius of $Tt1$ in $(A2)_8$
Ca_5Si_3	2.447(1)	−0.042	0.260	2.540	1.098	3.89	0.67	3.973	2.11
$Ca_5Si_3F_{0.4}$	2.435(2)	0.045	0.508	2.452	1.096	3.76	0.57	3.990	2.09
Sr_5Si_3	2.474(7)	0.044	0.277	2.688	1.096	4.12	0.71	4.205	1.96
$Eu_5Si_3H_x^a$	2.403(7)	0.112	0.625	2.495	1.069	3.89	0.61	4.103	1.91
Ca_5Ge_3	2.575(1)	−0.078	0.281	2.600	1.100	3.89	0.38	4.014	2.14
$Ca_5Ge_3H_x$	2.556(1)	0.081	0.686	2.362	1.076	3.67	0.47	4.063	2.10
$Ca_5Ge_3F_{0.66}$	2.568(1)	0.048	0.624	2.404	1.091	3.70	0.50	4.049	2.11
$Ca_5Sn_3H^b$	2.903(1)	0.048	0.829	2.391	1.063	3.75	0.39	4.316	2.25
$Ca_5Sn_3F_{0.9}^b$	2.910(1)	0.046	0.846	2.397	1.073	3.73	0.38	4.310	2.26
$Eu_5Sn_3H^{a,b}$	2.884(3)	0.038	0.640	2.550	1.050	4.03	0.54	4.453	2.21
$Sr_5Pb_3F^b$	3.106(3)	0.056	0.837	2.540	1.070	3.96	0.39	4.597	2.30
$Ba_5Si_3F_{0.2}^c$	2.442(6)	0.008, 0.160	0.448	2.765	1.078	4.29	0.73	4.253, 4.558	2.06, 2.11

[a]Consistent deviations; see text.
[b]Ref. (11).
[c]Primitive Ba_5Si_3-type cell (B).

appreciably smaller than those in other examples of each type and should probably be set aside. We will return to this aspect later.

Factors that allow this general constancy of $d(Tt2$–$Tt2)$ seem worthy of further exploration. The dimers are seen to run through the face that is common to a pair of trigonal prisms of $A2$ cations (one is highlighted in Fig. 2a), and a reasonable concern might be whether the dimer distances are influenced by matrix effects (crowding) from the cations. (Or better, why are they not more affected?) The $A2$–$Tt2$ distances occur in two categories, four equal values around the waist of the dimer (which lies on an inversion center) and two equal pair between the $Tt2$ atoms and the far edge of each antiprism. The differences between A–Tt distances at the end and waist of the trigonal prism, a conceivable source of a matrix effect, are given in col. **2** of Table 7. (Of course, the dimer is not electronically isotropic in these two directions.) In the one example with a large positive value, $Eu_5Si_3H_x$, reduced attractions to Eu^{2+} at the ends of Si_2^{6-} could conceivably cause the observed reduction in the Si-Si bond length, but this questionable attribution is not pertinent to the other Eu problem, a short Sn–Sn separation. A better electronic reason will be suggested later. The four A2 atoms about the waist of $(Tt2)_2$ actually define a rectangle, longer along $\vec{c}$, and the difference between the vertical and the horizontal edge is given in col. **3** for later reference.

The means by which not only the isolated $Tt1$ but also a potential small interstitial anion are accommodated in the other layer in this structure (Fig. 2b) further illustrate the versatility and specificity of this structure type. The effect of binding H^- relative to the empty version always decreases the size of the tetrahedral hole, whereas the relative variations in the lattice constants, in a/c, and in the proportions of the tetrahedra are somewhat diverse. Substitution of F^- for H^- always results in a smaller expansion, consistent with their comparative radii (37). The volume changes relative to empty phases were summarized in Table 6, and the radii of the approximate tetrahedra are given in Table 7, col. **4**. Variations in the proportions of the tetrahedra are enumerated in col. **5**, the ratio of side to top $A2$–$A2$ edges of the tetrahedra (viewed along $\vec{c}$), and col. **6**, the smaller top (and bottom) edge lengths alone (normal to $\vec{c}$), respectively. The nominal square antiprismatic surroundings about $Tt1$ are imperfect in that the alternating distances between the squares, around the edges of the figurative crown, are unequal, the smaller $A2$–$A2$ interplanar separation always being the side edge of the tetrahedron, Fig. 2b. The difference between these, col. **7**, Table 7, is identified as the "twist," the unshared minus the shared edge lengths. This varies with reapportionment of the tetrahedron and becomes less for larger Tt.

An interesting and relatively simple coupling between the tetrahedra and the sizes of the squares in the distorted $A2$ antiprisms about $Tt1$ can also be found. The latter naturally increase with the size of A, the size of Tt at fixed A, and with substitution of F and then H at fixed A and Tt. The first two are fairly straightforward size effects, while for fixed A and Tt sizes there is a simple mechanical coupling of the squares with the top edge of the tetrahedron, as marked in Fig. 4b. A decrease in the top and bottom edges on binding H or F is coupled directly to a twist of the antiprism, CCW (counter-

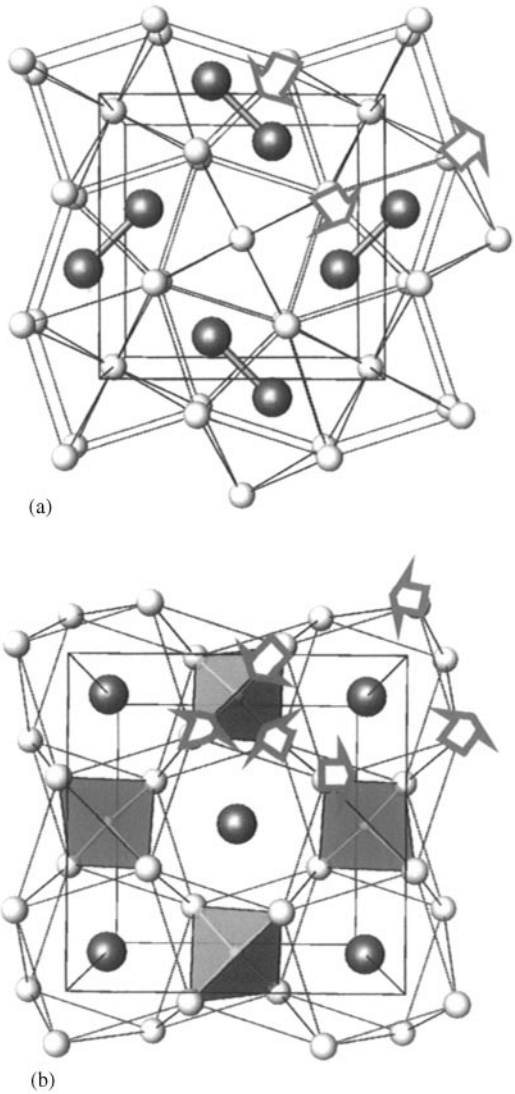

FIG. 4. Relative displacements of Ca2 in Ca_5Ge_3Z that accompany the binding of H or F in a smaller tetrahedron. (a) at $z = \frac{1}{2}$, around the Ge_2 units; (b) around $z = \frac{1}{4}$ in which only displacements of $A2$ in the top tetrahedral face and of the upper face of the square antiprism are marked.

clockwise, marked) in the top face and CW in the bottom, which simultaneously increase the length of the unshared side edge of the antiprism, col. **5**. Decreases in the side edges of the tetrahedron (those with components along $\vec{c}$) and a flattening of the antiprisms along $\vec{c}$ also follow increased bonding in the tetrahedron. The last occurs in a less predictable articulated way, although the flattening is naturally accompanied by increases in the size of the $A2$ squares for fixed A and Tt, col. **8**, Table 7, in order to maintain something near a fixed $d(A2–Tt1)$.

These articulated or coupled effects also extend to the other section of the structure that contains the dimer, a unique feature of this common structure type. The square faces of the antiprisms around $z = \frac{1}{4}$ are of course common to those of the $A1$-centered square prisms around $z = 0$, $\frac{1}{2}$. As shown in Fig. 4a, transmission of the twist in the former ($z = \frac{1}{4}$) to the further face of the square prisms centered around $z = \frac{1}{2}$ on interstitial binding changes the proportions of the face-shared antiprisms around Tt_2 too. This increases the distance between the $Tt2$ atoms and the end of the prism ($\times 2$), lessening any crowding there, and decreases the distance between the waist $A2$ and $Tt2$ ($\times 4$), Fig. 4a. This is as observed in the difference, col. **2**, Table 7. Note that the $A2–A2$ pair at the top of the tetrahedron and that across the waist of the dimer normal to $\vec{c}$ are *the same atoms*, Figs. 1, 2, accounting for part of the changes just elaborated.

These changes are also synchronized with a lengthening of $\bar{d}(A2–A2)$ around $z = \frac{1}{2}$ and parallel to c, the height of the trigonal prisms. Thus, a flattening of the tetrahedra and of the square antiprisms is accompanied by a significant increase in the other variable along $\vec{c}$, the overall $A2$-$A2$ heights of the layers around $z = \frac{1}{2}$, and thence of the trigonal prismatic pairs seen in projection around the waist of Tt_2. This means the four $A2$ atoms about the waist are disposed in an increasingly rectangular array. These edge differences in col. **3**, Table 7, are over 0.80 Å for the larger Tt with Ca and Sr. It is not clear that this increasingly anisotropic environment around the waist of Tt_2 has a significant effect, although it will split the degeneracies of the π levels on the dimers.

We suggest that the instabilities of binary A_5Tt_3 phases with empty tetrahedra for all Tt = Sn, Pb (except Sr_5Sn_3), but their stabilities as ternaries with bound hydride and, where tested, fluoride (Ca–Sn, Ba–Sn, Eu–Sn, Sr–Pb, Ba–Pb, Eu–Pb) (11), all arise because of the foregoing interrelationships. In other words, the absence of interstitial binding yields an inappropriate sizing of the pair of confacial $A2$ trigonal prismatic sites around the larger Tt_2, namely, with too-short $A2–Tt$ distances at the opposite ends of this figure, the reverse of the distortion marked in Fig. 4a. A forecast of this is seen in the large negative value of this difference for Ca_5Ge_3 in col. **2**, Table 7. Of course, instability is always with respect to an alterative, which in these cases is usually binary W_5Si_3-, $Pu_{31}Pt_{20}$-, or $Yb_{36}Sn_{23}$-type structures.

Finally, it is useful to estimate some radii for the tetrelide anions. Those for the dimers bound in the confacial trigonal prisms are defined by the two different values, about the waist and at the ends (Fig. 2a). These distances may not be very transferable, and there is also the problematic localization of high-lying π^* electrons on the Tt_2^{-6} dimers (below). On the other hand, distances between the isolated, nominal Tt^{-4} and $A2$ in the twisted antiprisms seem to represent something real and reproducible. For this purpose, col. **9** of Table 7 contains those radii deduced from $d(Tt1–A2)$ ($\times 8$) on subtraction of the six-coordinate crystal radii of

A^{2+} (39). The values obtained for Si, 1.96–2.11 Å, Ge, 2.10–2.14 Å, Sn 2.25–2.26 and Pb, 2.30 Å are $\sim$ 0.4, 0.3, and 0.2 Å larger than radii for the respective isoelectronic and much less polarizable halide anions, a reasonable trend for the increased polarizability of heavier *Tt*. (The smaller values for Eu salts are again omitted.)

3.5. Physical Properties

There is ample evidence that the parent A_5Tt_3 phases in the Cr_5B_3-type structure with dipositive cations are not the classical Zintl phases suggested by their structural components $(A^{+2})_5(Tt^{-4})(Tt_2^{-6})$, that is, with localized electrons on the anions as indicated. Instead, these phases exhibit both resistivities and paramagnetic susceptibilities indicative of metallic characteristics. Not surprising, the oxidized hydrides and fluorides thereof behave similarly. Figure 5 shows the resistivities measured by the "Q" method for Ca_5Ge_3 and $Ca_5Ge_3H_x$, both falling in the range of $\sim$ 30 to $\sim$ 70 $\mu\Omega$cm over the range shown with positive temperature coefficients (0.32(4) and 0.24(4)% K^{-1}, respectively), i.e., reasonable for poor metals. Figure 6 shows the fairly typical Pauli-like paramagnetic properties of Ca_5Ge_3 (189), Sr_5Ge_3 (163), and Sr_5Sn_3 (144) as well as of $Ca_5Ge_3H_x$ (7680), $Ca_5Ge_3F_x$ (585), with the room temperature χ value (10^{-6} emu mol^{-1}) for each in parentheses. (These results may of course include van Vleck TIP contributions.) The Ca_5Ge_3 sample was known to contain $\sim$ 5% CaGe (CrB type), which is presumably metallic, but this does not appear to have had a noticable effect at that level. The reason for

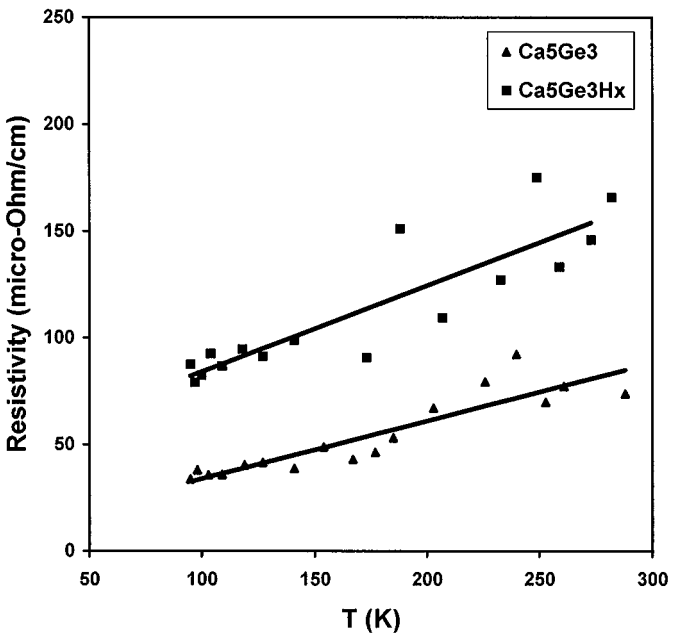

FIG. 5. Resistivity data for Ca_5Ge_3 (▲) and $Ca_5Ge_3H_x$ (■) as a function of T (K).

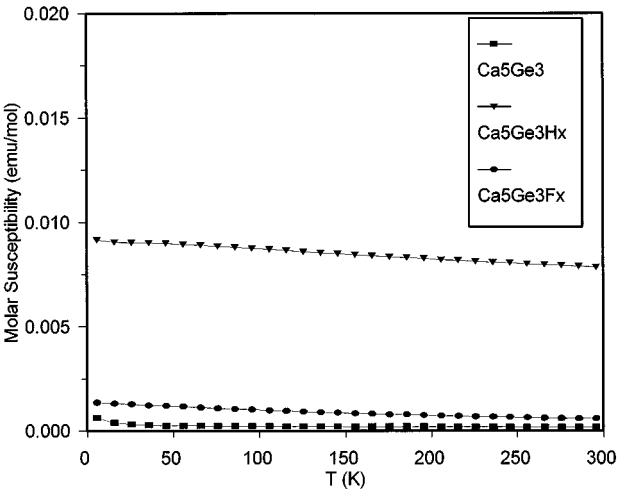

FIG. 6. Molar magnetic susceptibility data (χ) as a function of temperature for Ca_5Ge_3, (■), $Ca_5Ge_3H_x$ (▼) and $Ca_5Ge_3F_x$ (•).

the large elevation of the $Ca_5Ge_3H_x$ susceptibility is unknown. Similar Pauli-like results but with slightly larger increases in χ on cooling were reported earlier for $Ca_5Sn_3H_x$, $Ca_5Sn_3F_{0.9}$, and Sr_5Pb_3F with room temperature χ values (10^{-6} emu mol^{-1}) of 39, 53, and 350, respectively (11).

In contrast to the regular behavior of binary Sr_5Ge_3, sizeable temperature dependencies of the susceptibilities are found for the two strontium hydride phases $Sr_5Ge_3H_x$ and $Sr_5Sn_3H_x$, Fig. 7. The μ_{eff}(BM) and θ(K), parameters that fit these to the Curie–Weiss function drawn in (without TIP terms) are 1.67(5)/ $-$ 161 and 1.59(4)/ $-$ 64, respectively. The tin sample was epr silent at liquid N_2 temperature and above. Such behaviors for main-group element compounds are unusual and not understood.

4. GENERAL CONSIDERATIONS

The source of the metal-like properties of some, and probably all, of the binary A_5Tt_3 phases considered here is not hard to imagine. The formal closed-shell Tt_2^{-6} ions are isoelectronic with the following dihalogens, which are commonly described in terms of the p-orbital states $(\sigma_g^2)(\sigma_u^4)(\pi_g^{*4})$. Occupancy of localized antibonding states in a condensed solid salt would be problematic, and certainly less favored energetically than the idealized Tt^{-4} octet states (in a cation matrix, of course). At least some π^* electrons must be delocalized into the conduction band, so that the observed ready oxidations by hydrogen or fluorine are not really unusual given the clearly suitable means of accommodating a small interstitial in the structure. Possible oxide and nitride interstitials have not been explored in these systems except for negative results for $Ca_5Ge_3O_x$, but these are known in two other Cr_5B_3-type families, the electron-richer

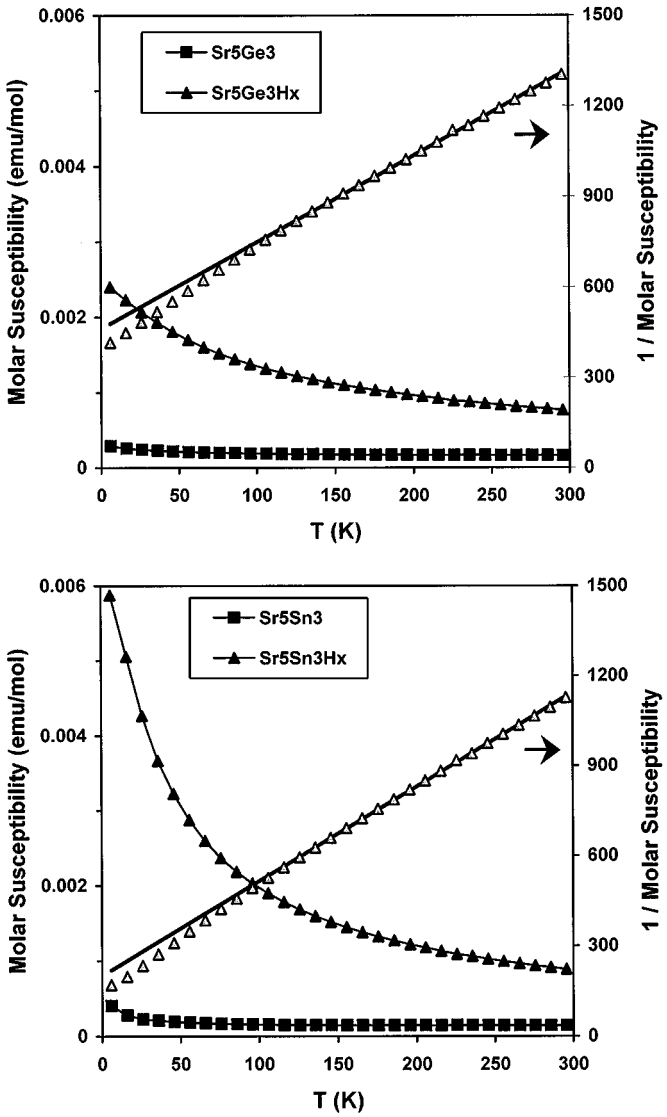

FIG. 7. Molar magnetic susceptibility data as a function of temperature. (top) Sr_5Ge_3 and $Sr_5Ge_3H_x$; (bottom) Sr_5Sn_3 and $Sr_5Sn_3H_x$. Data for the two hydrides are also shown as $1/\chi$ along with the best Curie–Weiss-type fits.

$La_5Pb_3(O, N)$ in which the lead dimers no longer exist (13) and in the isotypic KBa_4Sb_3O in which K substitutes for Ba1 (40). Extended Hückel band calculations for Ca_5Sn_3H, Ca_5Ge_3Z, etc., show, not surprisingly, that the Fermi energy lies within the antibonding π^* band (11, 34). However, the band results did not exhibit an appropriately low gap between valence and conduction bands because only default H_{ii} values were used that are more suitable for neutral or cationic triels. We surmise that the shorter distances observed for the Si–Si and Sn–Sn dimers when Eu is the cation (Table 7) (but not for $Eu_5Ge_3(H_x)$ (30)) arise because this cation-dominated conduction band lies lower than those for Ca, Sr, Ba, and more electrons from the anions' π^* states spill over into the conduction band. The presence of some Eu^{III} would not need to be contradictory in terms of π^* occupancies if the cation band were low enough, and this would also be consistent with the ~ 0.05–0.10 Å smaller values observed for the apparent radius of $Tt1$ (Table 7, col. **9**) for those two examples (as well as in $Eu_5Ge_3(H_x$ (30)). Magnetic data are not available for any of these europium salts.

A conceivable consequence of a real depopulation of the Tt_2 π^* states is that the lengths of the bonds should ideally decrease. However, the complexities of the close structural interrelationships already considered generate some caution that it could be this simple. Notwithstanding, the three cases for which we have Tt–Tt bond distances for both empty and stuffed examples with a fixed cation show small consistent decreases on oxidation (Table 7): Ca_5Si_3 to $Ca_5Si_3F_{0.4}$, by 0.012(2) Å; Ca_5Ge_3 to $Ca_5Ge_3H_x$, 0.019(1) Å, and to $Ca_5Ge_3F_{0.66}$, 0.007(1) Å. Of course, we know nothing about the actual degree of π^* depopulation and whether, or how, this changes with cation or Z; it is also possible that the differentiating electrons in these cases come from the conduction band. The picture is not so simple when $\bar{d}(Tt2$–$Tt2)$ in this structure type from other sources are included, even with impurity uncertainties. However, all reported Si–Si and Ge–Ge distances in this structure (except for Eu and those with lattice constant problems) fall in small ranges only 0.04 and 0.02 Å wide, respectively. In addition to this, we must have what are generally recognized as the effects of charge (and electron pair) repulsion in lengthening bonds in dimeric or other oligomeric anions (41). We have noted earlier that the Sn–Sn distances in two such phases (Table 7) are less than those for the dimers in the semiconducting Zintl phase $Ca_{31}Sn_{20}$ by 0.15 to 0.28 Å, whereas the homoatomic bonds in the element or in anionic network structures with lower charge densities and smaller repulsions are still shorter than in the present dimers (11).

Such a body of comparative information for the dimers is harder to find for the present silicides and germanides. The Si–Si and Ge–Ge bonds in the binaries reported here, ~ 2.45 and ~ 2.57 Å, are naturally longer than in the 4-bonded elements, 2.34 and 2.44 Å (42). The similarly bonded clathrate II network structures $A_8A'_{16}Tt_{136}$ evidently have some if not all of the electrons from a small number of cations in a conduction band, and those distances are slightly longer than in the elements, 2.36–2.39 Å and 2.49–2.51, respectively (43). Another concordant example is 2.50 Å between the only fully occupied Ge–Ge atom pair in Ba_6Ge_{24} (44). Differences from our results presumably arise because there are smaller charge and negligible lone pair repulsion effects in this last group. Likewise, the well-known tetrahedral anions Tt_4^{4-} presumably exhibit the effects of smaller charge repulsions, reduced electron pair repulsions, and perhaps angular strain, whereas the effects of cation alterations appear to be small. Distances in Si_4^{4-} in the

alkali-metal salts, $BaSi_4$, and Na_2BaSi_4 all fall in the range of 2.40–2.46 Å, actually in the lower half of the range except in RbSi and CsSi (45), and these differ surprisingly little from the distance in Ca_5Si_3, 2.45 Å, in spite of all the changes. The same is true for the analogous *A*Ge and $BaGe_2$ phases, 2.56–2.61 Å with a similar dependence on the nature of *A* versus 2.58 Å in Ca_5Ge_3 (46).

We will report later on a brief study of some analogous tetragonal A_5Tr_3 phases for the electron-poorer triels (Tr) Ga, In, and Tl (8). Significant in the present context, the reported thallide is actually stable only as $Sr_5Tl_3H_x$. In this case, the π^* band would ideally be empty for $x = 1$, and the Tl–Tl distance is indeed shorter than any reported before. The much lower π^* populations possible in the A_5Tr_3 examples may be important in the unusual stability of these triel phases if π^* populations in the dimers are at all germane to their description. There is also another group of tetrels for Sm_5Tt_3 and Yb_5Tt_3 that occur only with Mn_5Si_3-type structures, usually for both the binaries and ternary hydrides. These compounds perhaps contain some trivalent cations since all of the anions in this structure type are isolated, and electron deficient phases are generally not found among tetrelides, but this situation has not been verified.

ACKNOWLEDGMENTS

We thank J. Ostenson and D. K. Finnemore for the magnetic susceptibility measurements.

REFERENCES

1. S. Kauzlarich (Ed.), "Chemistry, Structure, and Bonding of Zintl Phases and Ions." VCH, Boca Raton, FL, 1996.
2. T. Hughbanks, *in* "Inorganometallic Chemistry" (T. Fehlner, Ed.), p. 291. Plenum Press, New York, 1992.
3. E. A. Leon-Escamilla and J. D. Corbett, *J. Alloys Compd.* **206,** L15 (1994).
4. E. A. Leon-Escamilla and J. D. Corbett, *J. Alloys Compd.* **265,** 104 (1998).
5. W.-M. Hurng and J. D. Corbett, *Chem. Mater.* **1,** 311 (1989).
6. C. E. Messer, *J. Solid State Chem.* **2,** 144 (1970).
7. J. D. Corbett, E. Garcia, A. M. Guloy, W.-M. Hurng, Y.-U. Kwon, and E. A. Leon-Escamilla, *Chem. Mater.* **10,** 2824 (1998).
8. E. A. Leon-Escamilla and J. D. Corbett, to be submitted.
9. R. W. Henning, E. A. Leon-Escamilla, J.-T. Zhao, and J. D. Corbett, *Inorg. Chem.* **36,** 1282 (1997).
10. B. Huang and J. D. Corbett, *Inorg. Chem.* **37,** 1892 (1998).
11. E. A. Leon-Escamilla and J. D. Corbett, *Inorg. Chem.* **40,** 1226 (2001).
12. A. K. Ganguli, A. M. Guloy, E. A. Leon-Escamilla, and J. D. Corbett, *Inorg. Chem.* **32,** 4349 (1993).
13. A. M. Guloy and J. D. Corbett, *Z. Anorg. Allg. Chem.* **616,** 61 (1992).
14. P. Böttcher, Th. Doert, Ch. Druska, and S. Bradtmöller, *J. Alloys Compd.* **246,** 209 (1997).
15. C. B. Magee, *in* "Metal Hydrides," (W. M. Mueller, J. P. Backledge, and G. G. Libowitz, Eds.), Chap. 6. Academic Press, New York, 1968.
16. P. Villars and L. D. Calvert, "Pearson's Handbook of Crystallographic Data for Intermetallic Phases," 2nd ed. American Society for Metals International, Metals Park, OH, 1991.
17. A. M. Guloy and J. D. Corbett, *Inorg. Chem.* **32,** 3532 (1993).
18. E. A. Leon-Escamilla, W.-M. Hurng, E. S. Peterson, and J. D. Corbett, *Inorg. Chem.* **36,** 703 (1997).
19. "TEXSAN, Single Crystal Structure Analysis Software," Version 5.0. Molecular Structure Corp., The Woodlands, TX, 1989.
20. J. T. Zhao and J. D. Corbett, *Inorg. Chem.* **34,** 378 (1995).
21. B. Eisenmann and H. Schäfer, *Z. Naturforsch.* **29B,** 460 (1974).
22. P. Manfrinetti, M. L. Fornasini, and A. Palenzona, *Intermetallics* **8,** 223 (2000).
23. G. Nargosen, G. Rocktäschel, H. Schäfer, and A. Weiss, *Z. Naturforsch.* **22B,** 101 (1967).
24. R. Nesper and F. Zuercher, *Z. Kristallogr., New Cryst. Struct.* **214,** 19 (1998).
25. K. Janzon, H. Schäfer, and A. Weiss, *Z. Naturforsch.* **21B,** 287 (1966).
26. R. Nesper and F. Zuercher, *Z. Kristallogr., New Cryst. Struct.* **214,** 20 (1999).
27. P. Pöttgen, R.-D. Hoffmann, and D. Kussmann, *Z. Anorg. Allg. Chem.* **624,** 945 (1998).
28. R. Nesper and F. Zuercher, *Z. Kristallogr., New Cryst. Struct.* **21,** 410 (1999).
29. R. Nesper and F. Zuercher, *Z. Kristallogr., New Cryst. Struct.* **214,** 22 (1999).
30. R. Pöttgen and A. Simon, *Z. Anorg. Allg. Chem.* **622,** 779 (1996).
31. W. Dorrscheidt, A. Widera, and H. Schäfer, *Z. Naturforsch.* **32B,** 1097 (1977).
32. G. Bruzzone, E. Franceschi, and F. Merlo, *J. Less-Common Met.* **60,** 59 (1978).
33. J. Harp, M. S. thesis, Iowa State University, Ames, Iowa, 1994.
34. E. A. Leon-Escamilla, Ph.D. dissertation, Iowa State University, 1996.
35. M. Notin, J. Mejbar, A. Bouhajib, J. Charles, and J. Hertz, *J. Alloys Compd.* **220,** 62 (1995).
36. A. M. Guloy and J. D. Corbett, *Inorg. Chem.*, to be submitted.
37. H. S. Marek and J. D. Corbett, *Inorg. Chem.* **22,** 3194 (1983).
38. R. Nesper and F. Zuercher, *Z. Kristallogr., New Cryst. Struct.* **214,** 21, 432, 413 (1999).
39. R. D. Shannon, *Acta Crystallogr. Sect. A: Found Crystallogr.* **32,** 751 (1976).
40. B. Eisenmann, C. Gieck, and U. Rössler, *Z. Anorg. Allg. Chem.* **625,** 1331 (1999).
41. R. Nesper, *Prog. Solid State Chem.* **20,** 1 (1990).
42. L. Pauling, "The Nature of the Chemical Bond," 3rd ed., p. 403. Cornell University Press, Ithaca, NY, 1960.
43. S. Bobev and S. C. Sevov, *J. Solid State Chem.* **153,** 92 (2000).
44. S.-J. Kim, S. Hu, C. Uher, T. Hogan, B. Huang, J. D. Corbett, and M. G. Kanatzidis, *J. Solid State Chem.* **153,** 321 (2000).
45. B. Huang and J. D. Corbett, *Solid State Sci.* **1,** 555 (1999).
46. J. T. Vaughey, G. J. Miller, S. Gravelle, E. A. Leon-Escamilla, and J. D. Corbett, *J. Solid State Chem.* **133,** 501 (1997).